ACS NANO

www.acsnano.org

ARTICLE

Giant Purcell Broadening and Lamb Shift for DNA-Assembled Near-Infrared Quantum Emitters

Sachin Verlekar,[○] Maria Sanz-Paz,[○] Mario Zapata-Herrera,[○] Mauricio Pilo-Pais, Karol Kołątaj, Ruben Esteban,* Javier Aizpurua, Guillermo P. Acuna,* and Christophe Galland*

Cite This: *ACS Nano* 2025, 19, 3172−3184

Read Online

ACCESS | Metrics & More | Article Recommendations | Supporting Information

ABSTRACT: **Controlling the light emitted by individual molecules is instrumental to a number of advanced nanotechnologies ranging from super-resolution bioimaging and molecular sensing to quantum nanophotonics. Molecular emission can be tailored by modifying the local photonic environment, for example, by precisely placing a single molecule inside a plasmonic nanocavity with the help of DNA origami. Here, using this scalable approach, we show that commercial fluorophores may experience giant Purcell factors and Lamb shifts, reaching values on par with those recently reported in scanning tip experiments. Engineering of plasmonic modes enables cavity-mediated fluorescence far detuned from the zero-phonon-line (ZPL)—at detunings that are up to 2 orders of magnitude larger than the fluorescence line width of the bare emitter and reach into the near-infrared. Our results point toward a regime where the emission line width can become dominated by the excited-state lifetime, as required for indistinguishable photon emission, bearing relevance to the development of nanoscale, ultrafast quantum light sources and to the quest toward single-molecule cavity QED. In the future, this approach may also allow the design of efficient quantum emitters at infrared wavelengths, where standard organic sources have a reduced performance.**

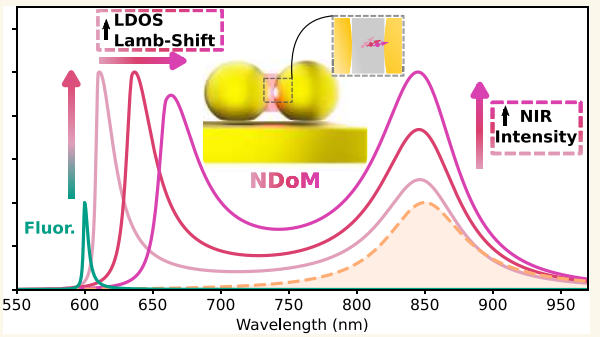

KEYWORDS: *single-molecule fluorescence spectroscopy, plasmonic nanocavities, DNA origami, single photon sources, Purcell effect, Lamb shift*

INTRODUCTION

Localized surface plasmon resonances (LSPRs) supported by metallic nanoparticles can be used to selectively enhance the scattering and absorption of light, allowing for the realization of optical nanoantennas.[1] When two nanoparticles, or a nanoparticle and a metal surface, are placed in close proximity, they can support LSPRs whose near field is tightly confined in the separating gap, thus forming plasmonic nanocavities.[2−4] Deep subwavelength field confinement in nanocavities allows for the engineering of light−matter interactions at the single-molecule level;[5−7] in particular, a quantum emitter placed in a nanocavity experiences a modified spontaneous emission rate, quantified by the local density of optical states (LDOS). In this context, a major enterprise has been to leverage the Purcell effect to increase the radiative decay rates of various quantum emitters coupled to plasmonic nanoantennas and nanocavities.[8−14]

For molecular emitters, which show multiple vibronic levels, coupling to LSPRs can significantly reshape their emission spectra when the LSPR is detuned from their zero-phonon line (ZPL), even without reaching the strong-coupling regime. The effect can be understood as the enhancement of decay rates for vibronic transitions that spectrally overlap with a broad plasmonic resonance. Previous systems employed to study spectral reshaping include lithographically fabricated arrays coated with emitters,[15−18] plasmonic antennas immersed in fluorophore solutions[19−23] as well as nanoparticles encapsulated by quantum emitters in a core−shell geometry.[24−27] More recently, spectral reshaping was studied at room temperature on single fluorophores immobilized close to the tip of gold nanorods using DNA origami.[28] The DNA-origami

Received: July 21, 2024
Revised: November 30, 2024
Accepted: December 9, 2024
Published: January 11, 2025

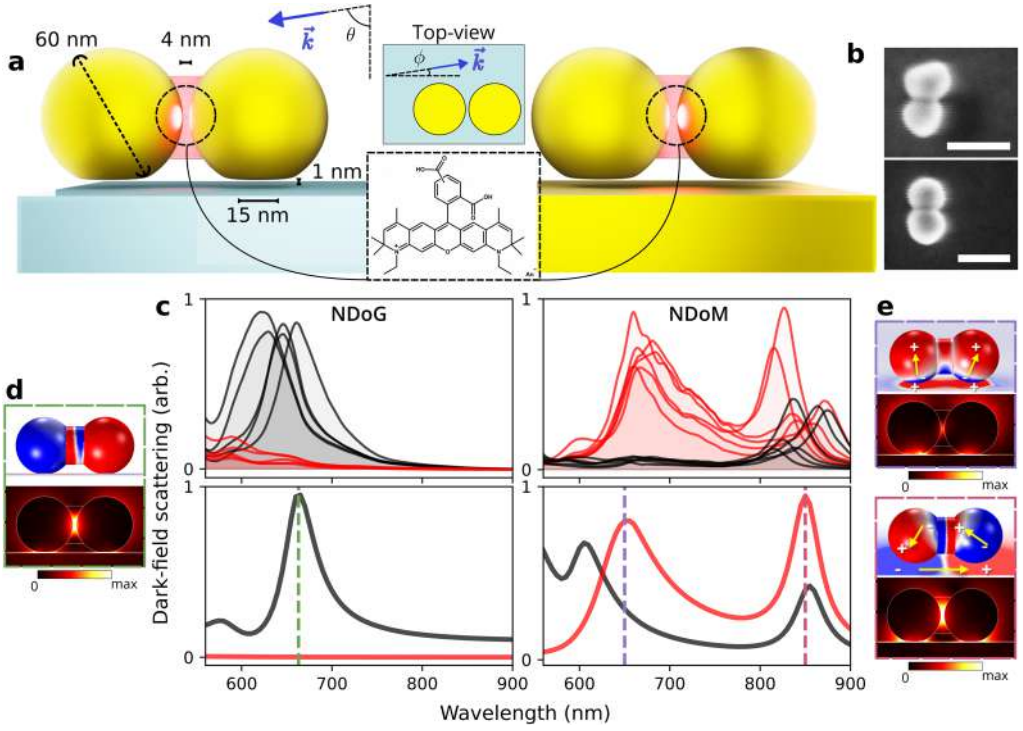

Figure 1. Optical dark-field characterization of nanocavities. (a) Illustration of NDoG (left) and NDoM (right) nanocavities. Relevant dimensions are shown, along with a blue arrow indicating the direction of white light used for polarization resolved dark-field scattering spectroscopy. The molecular structure of the ATTO 590 dye positioned in the gap between the two nanoparticles is shown as an inset. (b) Electron microscopy images of single NDoM nanocavities; the scalebars correspond to 100 nm. (c) Experimental dark-field spectra from individual NDoG (left) and NDoM (right) nanocavities at room temperature (top row) compared to the results of simulations using the geometry outlined in (a) (bottom row). Red lines correspond to *p*-polarized excitation, and black lines correspond to *s*-polarized excitation. In both experiments and simulations, an excitation angle θ of 81° with respect to vertical and a collection NA of 0.9 is used. For simulations, azimuthal angles (angle ϕ between the wavevector $\vec{k}$ and the dimer axis) of 90° and 10° are used for NDoG and NDoM respectively. (d) Simulated charge density (top) and near-field distribution (bottom) for the dominant radiative NDoG mode, at the wavelength indicated by the green dashed line in (c). (e) Simulated charge density and near-field distributions for NDoM modes, at the wavelengths indicated by the violet and red dashed lines in (c). (d,e) shows the enhancement of the electric field amplitude $|E/E_0|$, and the colormap is saturated to a maximum value of 20 in (d), 30 in the upper panel in (e), and 50 in the lower panel in (e). The charge density distribution is also saturated (both negative and positive values).

technique[29] allows for the bottom-up fabrication of 3D nanostructures[29−31] with dimensions on the order of tens to hundreds of nanometers and has found several applications in nanophotonics[32] as it enables the precise positioning of both metallic nanoparticles and single photon emitters with controlled orientation and stoichiometry.[33−35] Some notable examples include the enhancement of single photon emission,[36−40] surface-enhanced Raman scattering (SERS),[41−43] directing light,[44−46] ultrafast phenomena,[47] strong coupling,[48,49] and super-resolution microscopy.[50] In ref 28, pronounced reshaping of the light emission was demonstrated when the nanorod LSPR overlaps with the free-space fluorophore spectrum. While most results could be explained by the Purcell effect in the weak coupling regime through Fermi's Golden Rule,[24] some discrepancies were noticed[28] and attributed to a possible violation of Kasha's rule: because of the shortened excited-state lifetime, emission might also occur from excited vibrational sublevels.

All aforementioned studies were performed under ambient conditions so that the natural emission line widths largely overlapped with the plasmonic mode(s) involved in spectral reshaping, leaving open the question of whether emission can be induced well beyond the natural line width. Moreover, it is valuable to independently engineer the total vs the radiative LDOS: while the latter largely determines the reshaping function in the weak coupling limit, the former actually determines the change in the excited-state lifetime, with its possible impact on emission line width. In theory, a modified LDOS is also accompanied by a modification in the Lamb shift[51] (as they are connected to the imaginary and real part of the dyadic Green's function, respectively), but this effect has remained largely elusive in the context of plasmonic antennas, where it should however be particularly pronounced. Large Lamb shifts have been recently evidenced in a highly controlled environment, with a system consisting of free-base phthalocyanine molecules evaporated on monocrystalline silver films coated with bi- and trilayer NaCl and studied in an ultrahigh-vacuum, cryogenic scanning tunneling microscope.[52,53] Such systems contrast with the need for monolithic, solid-state (and ideally mass-producible) cavities that would fuel scalable photonic technologies, harvesting plasmonic LDOS control for the engineering of single emitter properties.

Here, we deterministically couple single commercial fluorophores to gold nanodimers (NDs) using DNA origami and study the resulting hybrid structures at cryogenic temperatures, where the ZPL of the bare fluorophore (as deposited on a glass slide) becomes much narrower than the plasmonic resonances and reaches a few meV. Plasmonic NDs

https://doi.org/10.1021/acsnano.4c09829
ACS Nano 2025, 19, 3172−3184

have been used in a number of experimental studies due to their directional far-field emission and giant field enhancement achieved in the narrow gap between the nanoparticles.[44,54−59] In order to obtain a highly radiative plasmonic mode in the near-infrared (NIR) region, far detuned from the fluorophore ZPL, we further utilize the interaction between the gold ND and a metallic substrate to form a nanodimer-on-mirror (NDoM) structure,[60−65] whose optical properties are compared to those of the nanodimer-on-glass (NDoG). These experimental improvements allow us to observe well-resolved and pronounced spectral reshaping of a single fluorophore emission. The fluorophore is seen to feed in the far-detuned NIR plasmonic mode of the NDoM, which does not spectrally overlap with the bare fluorophore emission. This NIR peak in fluorescence emission shows intensity fluctuations that follow the blinking dynamics of the fluorophore, while its wavelength and line width are stable over time, contrary to the wandering nature of the ZPL and associated vibronic shoulders.

We propose that feeding into the NIR mode of the NDoM at low temperatures is facilitated by a combination of the giant Purcell factor and Lamb shift. The Purcell effect leads to an inferred luminescence lifetime of only a few tens of femtoseconds that causes lifetime broadening of the fluorophore emission and enhances spectral overlap with the far-detuned NIR plasmonic mode. The Lamb shift contributes to pronounced red shifts (tens of meV) of the ZPL emission and works in synergy with Purcell broadening to increase the emission into the NIR mode. While our results are generally well reproduced by electromagnetic simulations of the photonic LDOS,[66] they also point out the need for a more accurate theoretical description of the joint dynamics of the nanocavity field and the molecular vibronic transitions, at the microscopic level. This would enable to fully capture this regime of light−nanomatter interaction now accessible with nanocavity molecular emitters, where electronic, photonic, and vibrational degrees of freedom all interact strongly with each other.[67−70] Our findings evidence the open questions and challenges in the control and understanding of nanocavity-coupled molecular emitters and may have broad implications for nanoplasmonic approaches to quantum optics and cavity QED.[5,48,71−73]

RESULTS AND DISCUSSION

With the help of rectangular DNA-origami structures (60 × 50 nm^2), a single ATTO 590 molecule (the fluorophore) is precisely positioned between two Au nanospheres (60 nm nominal diameter), forming the plasmonic nanocavity with gap width $g \approx 4-5$ nm (as expected from the total DNA-origami thickness); see Figure S1. Following their colloidal synthesis in solution (see Methods), NDs are deposited either on glass (NDoG; left panel in Figure 1a) or on a template-stripped gold substrate acting as a mirror (NDoM; right panels in Figures 1a and 1b). The ND is separated from the gold or glass substrate by single-stranded DNA sequences that are used to functionalize the Au nanoparticles with a thickness of ≈1−1.5 nm. We utilize two control samples consisting of the fluorophore-origami complex deposited directly on glass or being attached to a single Au nanoparticle before deposition on glass (NPoG, nanoparticle-on-glass).

The plasmonic resonances of individual nanocavities containing single fluorophores are investigated via dark-field scattering spectroscopy (Figure 1c). By dispersing NDs on the substrate with a very low surface density, we ensure that the scattering signal arises from a single nanostructure, as confirmed by electron microscopy on a subset of points, which also confirms that we can differentiate between dimers and monomers by their far-field scattering intensities (Figure S2). The optical responses of these configurations are calculated using electromagnetic simulations (Methods and Supporting Information). The measured (top row) and calculated (bottom row) spectra in the left columnFigure 1c show that the dominant radiative mode of the NDoG lies in the visible region (∼620−670 nm), which overlaps well with the fluorophore ZPL ($\lambda_{em} \simeq 622$ nm at 300 K). The NDoG shows strong scattering only under *s*-polarized illumination (labeled with respect to the substrate, black lines in Figure 1c), dominated by the bonding dipolar plasmon (BDP) mode along the dimer axis (see charge and field distribution in Figure 1d). This mode is excited by the s-polarized illumination because the propagation direction is chosen perpendicular to the dimer axis.

In the NDoM configuration, the BDP mode is strongly red-shifted toward the NIR region (wavelength ≥800 nm) due to the interaction with the metallic substrate, as shown experimentally and by calculations (Figure 1c, right column). This red-shifted mode can be excited by *s*- and *p*-polarized illumination and is characterized by strong surface charge concentration in the three gaps forming the structure (one gap between the two spherical nanoparticles and two gaps between the dimer and the gold substrate), as illustrated by the corresponding charge and field distributions in Figure 1e.

The NDoM dark-field scattering spectrum also shows a mode in the visible (VIS) domain (630−700 nm, Figure 1c), of a different nature compared to the main radiative BDP mode of the NDoG cavity. This mode can only be excited by *p*-polarized excitation and is characterized by strong surface charge and field enhancement at the gaps between the ND and the metallic substrate, but not in the gap between the two spherical nanoparticles forming the dimer, where the fluorophore is to be located (the relatively strong local field in these spots in Figure 1e is due to contributions from other plasmonic modes). The difference in field strength at the fluorophore position compared to the NIR mode is due to the different field symmetry at the ND−substrate gaps. In the VIS mode, the orientation of the fields is the same in both gaps, but it is the opposite in the NIR mode. With generality, modes exhibiting a large field concentration at the gap between nanoparticles (BDP mode in NDoG and NIR mode in NDoM) enable strong radiative enhancement of a dipolar source placed at that position. This enhancement is comparatively weak for the NDoM mode at visible frequencies, but in this case, a large enhancement of the decay rate is still feasible as a consequence of the coupling with weakly radiative higher-order plasmonic modes typically responsible for quenching (see below).

These general spectral trends can be observed in all of the measured particles (Figure S3) and are correctly reproduced by numerical simulations of the optical response (see Figure S4 for details on the geometry and Figure S5a for additional simulation results). The large variation in the NIR mode position in experiments may arise from the variation in nanoparticle shape and DNA coverage, as corroborated by simulations (Figure S5a). We note that another strategy to red-shift the NDoG resonance would be to shrink the interparticle distance;[43] however, narrower gaps are challenging to achieve

https://doi.org/10.1021/acsnano.4c09829
ACS Nano 2025, 19, 3172−3184

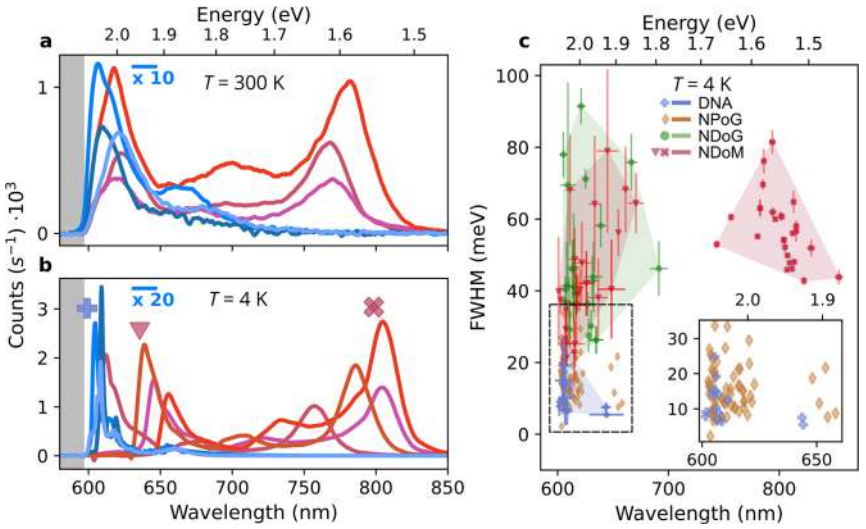

Figure 2. Spectral reshaping at ambient and cryogenic temperatures. Typical experimental emission spectra from single molecules in their DNA scaffold deposited on glass (blue curves) or embedded in NDoM cavities (shades of red) at room (a) and cryogenic (b) temperatures *T*. A long-pass filter cuts the emission below 600 nm. All spectra are measured under 590 nm excitation at 10 μW incident power (continuous wave) focused through a 0.82 numerical aperture (NA) with an acquisition time of 1 s (see Methods for further details). (c) Summary of emission line widths and positions of emission peaks at *T* = 4 K. The various groups are plotted with different markers, as indicated in (b) and in the legend. For fluorophores in NDoM (red symbols), the ZPL and far-detuned NIR emission are analyzed separately. The marginals of the data shown in (c) are presented in S10. Shaded areas are guides for the eye.

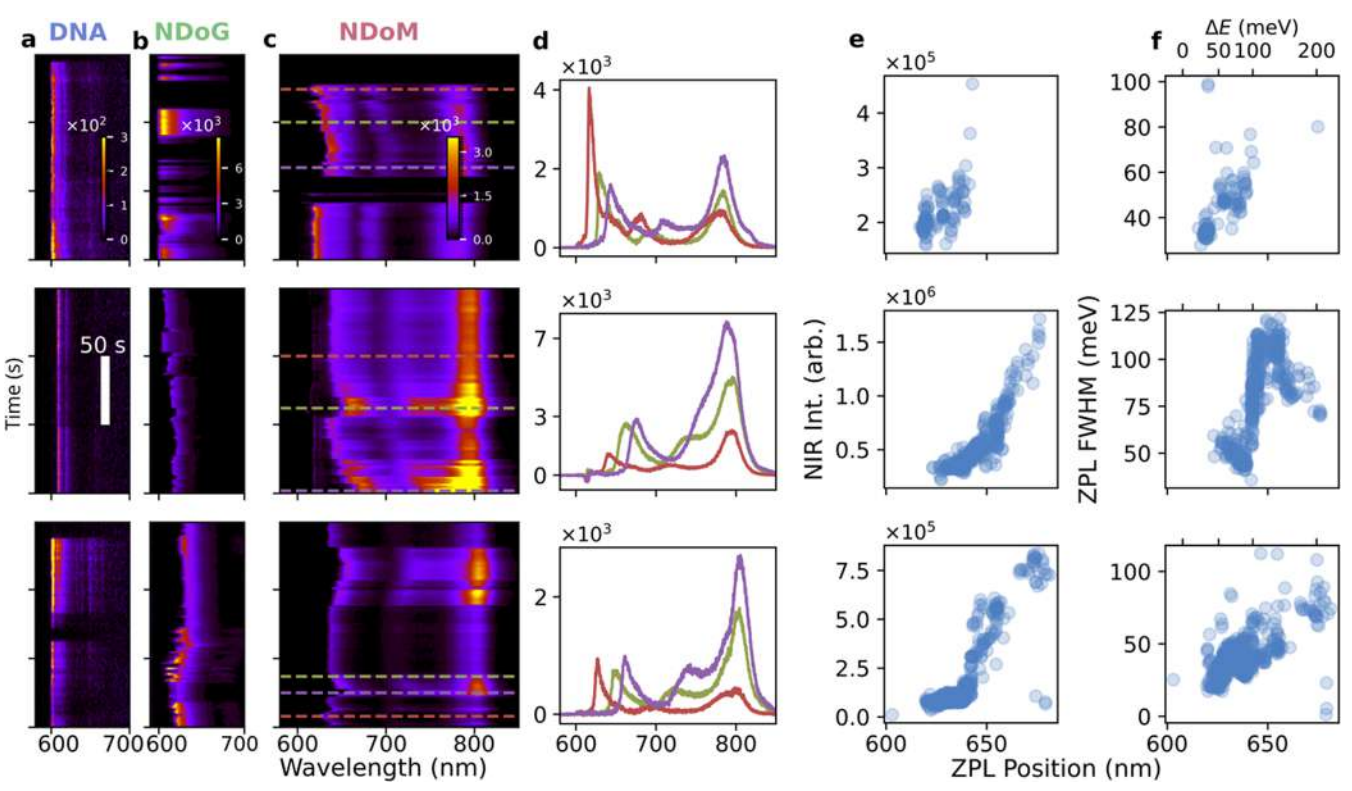

Figure 3. Spectral and intensity fluctuations. (a–c) Examples of typical time series of fluorescence spectra. Each column contains three individual emitters from one of the sample families presented in Figure 2c: bare fluorophore in DNA (first column), fluorophore in NDoG (second column) and fluorophore in NDoM (third column). The white bar in (a) indicates the common time scale, with time evolving from bottom upwards in each panel (a), (b) and (c). The full time series can be found in Figure S14. (d) NDoM spectra from the time points marked by lines in the time series in (c), highlighting the correlation among the ZPL position, NIR mode intensity, and ZPL line width. (e,f) Correlation plots of the ZLP position versus the emitted intensity at the NIR region (integrated from 700 to 900 nm) (e), and versus the FWHM (f), as extracted from each frame of the NDoM time series shown in (c).

using the DNA-origami approach, while they could also lead to stronger nonradiative quenching of fluorophore emission.[74] In addition, we will show that our dual-mode strategy allows for maintaining a high total LDOS at the ZPL frequency together with the highly radiative NIR mode.

https://doi.org/10.1021/acsnano.4c09829
ACS Nano 2025, 19, 3172–3184

We then perform fluorescence spectroscopy on individual structures at room and cryogenic temperatures to study light−matter interaction at the single-molecule level (see Methods for the apparatus). All samples containing the ATTO 590 fluorophore are measured using an excitation laser at 590 nm and a long-pass filter that allows us to collect fluorescence beyond 600 nm. The bare ATTO 590 fluorophore (i.e., in the absence of ND) has a broad emission line width at room temperature with a ZPL at $\lambda_{em} \simeq 622$ nm (Figure 2a, blue lines), along with a shoulder corresponding to vibronic sidebands. Upon measuring the fluorescence from bare individual molecules at $T = 4$ K bath temperature, we observe much narrower (∼10 meV) and asymmetric emission spectra because of the reduced thermal occupancy of vibrational modes and phonon bath,[75] as shown by the blue lines in Figure 2b and blue crosses in Figure 2c (see Figure S11 for more spectra). Results from NPoG nanocavities are shown with golden diamonds in Figure 2c (see Figure S12 for example spectra). These structures present a smaller Purcell factor than NDoG and NDoM (2−3 times lower; see Figure S8); however, a similar Lamb shift is expected due to the interaction of the emitter with its image dipole in the nearby metal.

The first major finding of our experimental study is illustrated by the red curves in Figure 2a,b, corresponding again to measurements at $T = 300$ K (Figure 2a) and $T = 4$ K (Figure 2b). When a fluorophore is embedded in an NDoM cavity, we observe not only a hundred-fold enhancement of spectrally integrated emission intensity (Figure S9a), consistent with an increased excitation rate, and an even larger enhancement of the total photon budget (Figure S9b), consistent with an increased decay rate,[76,77] but also a dramatic reshaping of the emission spectrum with two main features: (i) a significantly broadened and red-shifted ZPL (also seen for fluorophores in NDoG, shown in Figure S13), and (ii) the appearance of a strong peak around 750−800 nm, detuned from the original ZPL by ten to hundred times the main emission peak line width at $T = 4$ K. To our knowledge, such a pronounced reshaping of single-molecule emission has not been reported before. It is reminiscent of the phenomenon of "cavity-feeding" from far-detuned quantum emitters observed with epitaxial quantum dots strongly coupled to photonic cavities,[78−82] yet we do not expect our system to be in the strong-coupling regime.

A summary of the main spectral features from the set of investigated individual emitters is presented in Figure 2c, extracted from a time series of single particles measured at $T = 4$ K until photobleaching of the fluorophore. From each time series, the position and line width of the ZPL and NIR emissions are extracted and the mean value is represented by a point in Figure 2c. We keep using the term ZPL to denote, in this context, the highest energy emission peak in its entirety. Error bars are obtained by calculating the standard deviation over each measurement, while the shaded regions are guides only to the eye. A large spread of line widths is observed for the fluorophore ZPL in NDoG and NDoM nanocavities. This is assigned to the sensitive dependence of the Purcell factor and the Lamb shift on the exact geometry of the dimer (Figure S6c,d), on the position (Figure S7) as well as the orientation of the fluorophore (Figure S6a,b), as will be developed below.

Before modeling the reshaped, Purcell-enhanced emission, we study the spectral and intensity fluctuations (conventionally referred to as fluorescence wandering and blinking, respectively) from the three types of samples at low temperatures. These fluctuations are illustrated by a few emission time series in Figure 3a−c. For each measured emitter, the intensity, peak position, and full width at half-maximum (FWHM) are extracted frame by frame while separately treating the ZPL (at visible wavelengths) and cavity-enabled NIR emission for NDoMs. These quantities are then used to compute their respective levels of fluctuation over time, expressed through a boxplot in Figure S14b, and also study correlations from individual traces as discussed later. In these measurements, we benefit from the prolonged duration (several minutes) before the photobleaching of fluorophores, which is a combined effect of cryogenic temperature and plasmon-accelerated decay rate.[76,83]

On the one hand, we observe similar levels of relative intensity fluctuations across all sample types, which contrasts with earlier observations on colloidal quantum dots coupled to metallic structures[84−86] where faster decay has been reported to suppress blinking and stabilize emission intensity.[87] On the other hand, the observed spectral fluctuations of the ZPL are significantly enhanced when embedding the fluorophore in a nanocavity, be it an NDoG or NDoM. The magnitude of wandering of the ZPL is 4 or 5 times more pronounced on average compared to fluorophores in DNA on glass, with some nanocavities featuring spectral excursions larger than 30 meV (S14b). As illustrated by the spectra shown in Figure 3d and summarized in Figure 3e, when the ZPL wavelength shifts to longer wavelengths, the NIR emission intensity increases. The full traces are shown in Figure S17. The peak appearing in the region around ∼700 nm, seen clearly in Figure 3c spectrally wandering with the ZPL, is assigned to the vibronic sidebands of the molecule.

In contrast to the wandering fluorophore ZPL, the NIR emission shows a very stable center wavelength and line width (S14b), both governed by the plasmonic mode. After the fluorophore has bleached, the much weaker collected signal originates from the intrinsic gold luminescence from the nanocavity, whose spectrum can be used to accurately infer the plasmonic resonant modes (Figure S15).[88−91] This faint postbleaching gold luminescence shows a peak at the exact same position as the detuned NIR fluorophore emission, confirming the presence of the corresponding plasmonic mode at the single particle level. All of these observations support that the NIR emission is a consequence of the nanocavity mode being fed by the fluorophore emission.

Another interesting correlation can be observed in Figures 3f and S16: when the ZPL line width broadens, the ZPL emission typically red shifts. This correlation is consistent with both effects having a common cause, which we attribute to either a transient change in the effective molecule−gold distance or a change in molecular orientation, possibly resulting from instabilities in the neighboring gold surface configuration.[92] We indeed show in Figure S7 and Figure S6a,b that decreasing the molecule−gold distance or changing the dipole orientation in the simulation strongly affects both the Purcell broadening and the Lamb shift in a correlated manner. These correlations offer support for the role of Purcell broadening in the observed emission spectra. We describe in more detail below how this hypothesis is supported by theoretical modeling and tested by additional experiments with a different fluorophore (ATTO 643).

We begin by showing with electromagnetic modeling of the system that the Purcell effect and Lamb shift together with the presence of the NIR cavity mode can account for the main

https://doi.org/10.1021/acsnano.4c09829
ACS Nano 2025, 19, 3172−3184

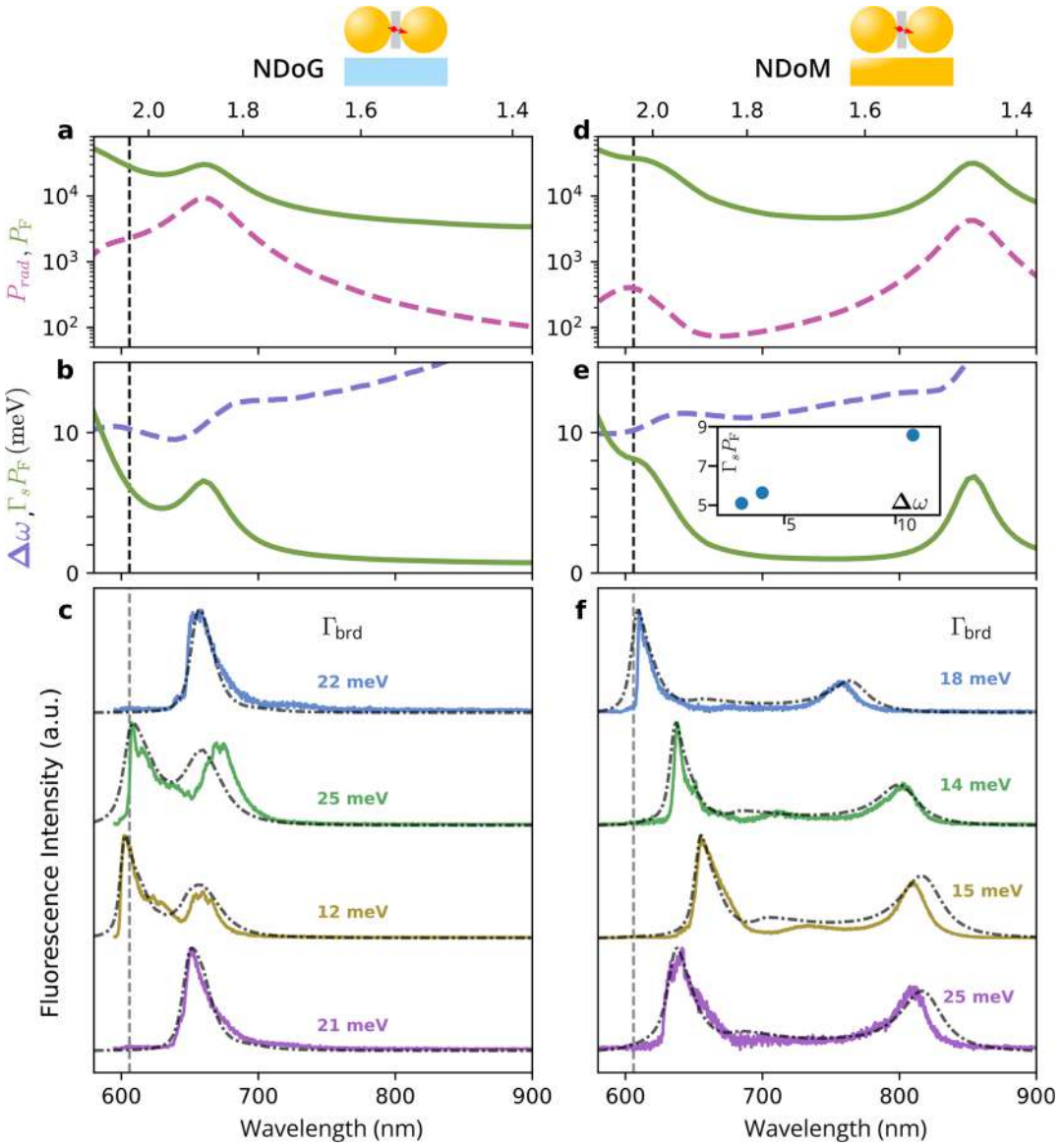

Figure 4. Modeling fluorescence reshaping. The two columns correspond to identical simulations and analysis performed for NDoG (left column) and NDoM nanocavities (right column). (a) Simulated radiative (P_{rad}, dashed line) and total (P_F, solid line) decay rate enhancement factors as a function of wavelength; and (b) corresponding Purcell broadening ($\Gamma_s \times P_F$) and Lamb shift ($\Delta\omega$) in meV, for a spontaneous emission rate (Γ_s) in the DNA of 1/3 ns^{-1}. Electromagnetic simulations are performed using the geometry sketched in Figure 1a (for NDoG and NDoM, respectively) with the dipolar emitter placed 1 nm away from one of the Au surfaces. The vertical dashed line in all panels indicates the average measured ZPL frequency of ATTO 590 in DNA origami on glass at 4 K. (c) Examples of experimental instantaneous fluorescence spectra (solid lines) along with estimates from the convolution model of eq 5 (dashed lines). The values shown next to each curve (in the corresponding color) are the values of Γ_{brd} obtained from the fit. Panels (d−f) show the same analysis repeated for NDoM nanocavities. The inset in (e) shows the correlation between the calculated frequency shift and Purcell broadening at the ZPL frequency for various locations of the fluorophore within the nanogap (additional data shown in Figure S7). The same molecular emission spectrum, $\mathcal{L}_{mol}^{ref}$, spectrally shifted to correctly match the ZPL position, is used in all examples. The appropriate P_{rad}, correctly matching the NIR mode position (see Figure S5b), is used for each NDoM case, while an identical P_{rad} is used for all NDoG examples. The dashed vertical line shows the average value of ZPL energy measured from bare fluorophores in origami.

experimental features of the NDoM system: the pronounced ZPL broadening, the transfer of emission intensity to the NIR peak, and the correlated fluctuations reported in Figure 3, while also reproducing the measured NDoG spectra with the same model. The NPoG system is a useful control in this regard since the distance between the fluorophore and the gold surface is maintained (∼1 nm), while the Purcell factor is significantly reduced. Since the NPoG does not have an additional LSPR mode in the region of interest (∼600−900 nm), experimentally we only see a slight broadening of the ZPL on average (∼7 meV), while the spectra remain qualitatively the same as the fluorophore in DNA (see the inset of Figures 2c and S12). Electromagnetic simulations predict a 2−3 times lower Purcell broadening for NPoG compared to NDoM, but similar Lamb shifts, because the latter arises mainly from the proximity of the dipole to the Au surface. The simulated Purcell broadening and Lamb shifts for NPoG (see Figure S8) are comparable, on average, with the

https://doi.org/10.1021/acsnano.4c09829
ACS Nano 2025, 19, 3172−3184

observed ZPL line width and wavelength distributions of Figure 2c. These observations hint at the electromagnetic origin of the observed broadening and reshaping, which we now investigate for the ND structures.

For NDoG and NDoM cavities, the radiative and total (including nonradiative) decay rates are numerically calculated by modeling the fluorophore as a point-like dipole located in the ND gap, along and parallel to the ND long axis and placed 1 nm away from one nanoparticle (consistent with the DNA-origami design); the results are plotted in Figure 4a (NDoG) and Figure 4d (NDoM) (see Figure S6 for the perpendicular configuration), for a spontaneous decay rate of the emitter in DNA of 1/3 ns^{-1}. The calculations and other considered geometries are described in more detail in the Methods section and in Figure S4. Two features of the NDoM should be highlighted: first, at the ZPL wavelength of ATTO 590 in DNA, which is around 600 nm at 4 K (cf. Figure 2c), the Purcell factor (shown in Figure 4d, green line, and defined as the increase in the spontaneous decay rate due to the presence of the ND) reaches $\sim 4 \times 10^4$, while its value is 3−4 times smaller around the ZPL of ATTO 643 that will be studied later. Second, the simulation confirms the presence of the NIR mode featuring both a large Purcell factor ($\sim 3 \times 10^4$) and a high radiative efficiency ($P_{rad}/P_F \sim 20\%$) close to 800 nm. In the case of NDoG, plotted in Figure 4a, a similar Purcell factor is obtained at the ATTO 590 ZPL wavelength with a dominant radiative mode (~30% efficiency) around 650 nm. These calculations are then combined with experimental data to model the observed reshaped fluorescence spectra.

A naive prediction of the modified fluorophore emission spectrum in a nanocavity, $\mathcal{S}(\omega)$, is given by the measured bare fluorophore spectrum $\mathcal{L}_{mol}(\omega)$ (examples shown in S11) multiplied by the radiative rate enhancement factor for a dipole in the nanocavity gap ($P_{rad}(\omega)$, dashed curve in Figure 4a,d) according to[24]

$$S(\omega) \simeq \mathcal{L}_{mol}(\omega) \times P_{rad}(\omega) \tag{1}$$

This approach, which was used with some success to model room-temperature data[24,28] (see Figure S18a), totally fails to reproduce the increased ZPL emission line width for a fluorophore embedded in NDoG or NDoM at low temperatures (see Figure S18b); as a result, it also predicts negligible NIR emission for fluorophores in NDoM. We therefore refine the model by accounting for the reduced luminescence lifetime of a fluorophore coupled to a nanocavity, which results in a broadened ZPL. When the emitter is modeled by a two-level system, its emission spectrum in a reference environment can be modeled by a Lorentzian function. Using the formalism in[93,94] with the frequency-dependent Purcell factor ($P_F(\omega)$) and Lamb shift ($\Delta\omega(\omega)$) inside the cavity, the fluorophore response is modified as

$$\mathcal{L}^{cav}_{mol}(\omega) = \frac{1}{\left(\omega - \omega_0 + \left(\frac{2\omega_0}{\omega+\omega_0}\right)\Delta\omega(\omega)\right)^2 + \left(\frac{2\omega_0}{\omega+\omega_0}\right)^2\left(\frac{(\Gamma_{deph}+\Gamma_{cav}(\omega))}{2}\right)^2} \tag{2}$$

where ω_0 is the central emission frequency in the absence of a cavity, Γ_{deph} is the pure dephasing rate (that vastly dominates the line width of the bare fluorophore), and $\Gamma_{cav}(\omega) = P_F(\omega)\Gamma_s$ is the Purcell enhanced decay rate (and corresponding broadening) inside the nanocavity, with the spontaneous radiative decay rate of the bare fluorophore Γ_s (Figure S19).

Finally, the photoluminescence signal of the coupled system is calculated by

$$\mathcal{S}^{cav}(\omega) = \mathcal{L}^{cav}_{mol}(\omega) \times P_{rad}(\omega) \tag{3}$$

In this model, all vibrational degrees of freedom of the molecule are phenomenologically included into the pure dephasing rate Γ_{deph}. However, as the low-temperature fluorescence spectra feature asymmetric ZPL and vibronic sidebands, the two-level approximation must be improved upon. We introduce a heuristic model based on the convolution of the reference fluorophore spectrum with a Lorentzian function that accounts for Purcell broadening through the broadening parameter Γ_{brd}, which can be identified with the predicted value of $P_F\ \Gamma_s$ close to the Lamb-shifted ZPL energy:

$$\mathcal{L}^{brd}_{mol}(\omega) = \int \mathcal{L}^{ref}_{mol}(\omega - \omega'; \omega_{shift}) \frac{\Gamma_{brd}/2}{\pi((\Gamma_{brd}/2)^2 + (\omega')^2)} d\omega' \tag{4}$$

In the following, we chose the fluorophores in DNA dispersed on glass as the reference $\mathcal{L}^{ref}_{mol}$. When attached to gold nanoparticles, the shift of the fluorophore takes a range of values so that we introduce a spectral shift by hand (ω_{shift}) to match the ZPL positions of the reference to the emission in the presence of the nanocavity. We use this frequency shifted reference ($\mathcal{L}^{ref}_{mol}(\omega; \omega_{shift})$) and determine the Γ_{brd} that results in the best fit to the reshaped spectra, which is defined by

$$\mathcal{S}^{brd}(\omega) = \mathcal{L}^{brd}_{mol}(\omega) \cdot P_{rad}(\omega) \tag{5}$$

The predictions of this improved heuristic model, shown in Figure 4c,f, allow us to recover the correct line shape for the ZPL in both NDoG and NDoM while also being able to predict the correct NIR intensity for NDoM, with values of Γ_{brd} that are comparable (within a factor of ~4) to the predicted lifetime broadening through the Purcell effect using a fluorophore spontaneous decay rate (Γ_s) of 1/3 ns^{-1}, very close to that measured in Figure S19. We acknowledge that the values of Γ_{brd} obtained from our fits are larger than the predicted values of Purcell broadening from the simulations, even under the assumption of an optimal dipole alignment. It must be noted that the dipole is unlikely to be substantially misaligned since this would lead to quenching of radiation, but a small deviation from the dimer axis does result in reduced coupling strengths, exacerbating the discrepancy.

Multiple factors that are not accounted for in our simplistic model may contribute to the discrepancy, such as nonlocal effects of the metallic response,[95−97] the lack of knowledge of the exact geometry and atomistic protuberances or picocavity events.[98] To further study the role of picocavities and atomic-scale fluctuations in the nanogap, we reproduce a recent experimental study[92] that induced picocavities in similar DNA-origami constructs under higher laser powers and attributed a facilitating role to the fluorophore in picocavity formation. Our data (see Figure S20) additionally show that the dimer gap shrinks at high laser power, possibly due to heat-induced shrinking of DNA as reported in ref 43. Picocavities or other field-enhancing features may also randomly occur at low laser power and would lead to transiently higher Purcell factors[99]—a phenomenon not included in our model. Even with our simple assumptions, the Purcell model captures some of the essential features of the system while broadly reproducing the experimental observations.

https://doi.org/10.1021/acsnano.4c09829
ACS Nano 2025, 19, 3172−3184

To further test our hypothesis regarding the importance of Purcell broadening, we investigated a second set of nanocavities that host a different fluorophore (ATTO 643, Figure 5). As seen from the bare fluorophore spectra (Figure S11),

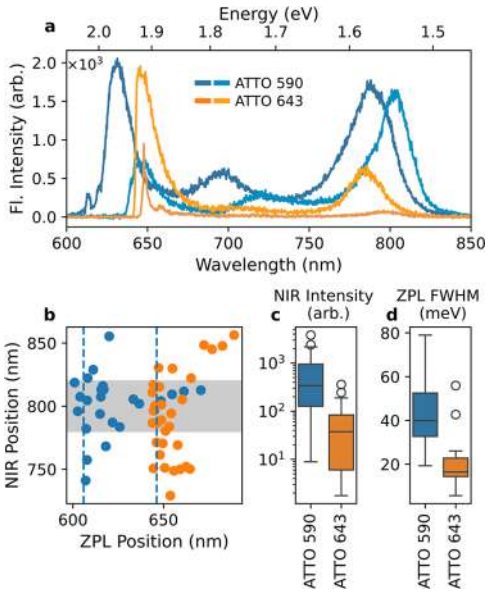

Figure 5. Experimental comparison of Purcell broadening and NIR emission for two different fluorophores. (a) Examples of typical fluorescence spectra from NDoMs containing individual ATTO 590 (shades of blue) and ATTO 643 (shades of orange) fluorophores. (b) Scatter plots showing the measured ZPL and NIR emission wavelengths for the two sets of NDoM samples containing different fluorophores. (c) Statistics of NIR emission and (d) ZPL FWHM of the selected subset of nanocavities that have an NIR mode wavelength between 780 and 820 nm, indicated by the shaded region in (b).

ATTO 643 ZPL (average ZPL emission wavelength ~646 nm at 4K) is red-shifted compared to ATTO 590 (~606 nm). However, even though ATTO 643 is tuned closer to the NIR mode, the observed NIR intensity is weaker on average (Figure 5c), which we attribute to lower Purcell broadening. Indeed, by choosing a subset of all measured samples that may have a similar geometry (based on their plasmonic NIR resonances, gray strip in Figure 5b), we find that the ZPL line width is significantly narrower for ATTO 643, as shown in Figure 5d (see also Figure S21a), which is in line with the NDoM simulations predicting a lower total Purcell factor around 650 nm compared to 600 nm (Figure 4d). Note that this trend is robust and visible without any postselection (Figure S21 and Figure S22). Altogether, the fluorophore that is detuned further from the NIR mode is feeding it more efficiently, in accordance with our model that accounts for giant Purcell broadening and Lamb shift at the single-molecule level.

While this model seems to capture the essential physics at play, several other mechanisms will require future investigations. In particular, the predicted total Purcell factor corresponds to a shortening of the emission lifetime of approximately 100 fs. Under such rapid decay, Kasha's rule, which states that emission always occurs from the lowest vibrational level of the excited electronic state, could be violated.[28,100] Since the Franck–Condon factors from vibrationally excited levels may substantially differ from those involving the lowest level, it is unclear what the actual spectrum would be in this case (we would naively expect emission at higher energies, which does not seem to occur). Testing this hypothesis may require ultrafast transient measurements with a temporal resolution of a few tens of femtoseconds on single nanocavities.[101,102] On the theoretical side, there is interest in solving a model that nonperturbatively accounts for the coupling of the electronic states to the molecular vibrations and to the dynamically screened electromagnetic field while properly describing all dissipation channels. A few recent works can serve as a basis for this extension.[67,103] It is possible that the additional terms coming from the Purcell effect acting on the vibronic states can more accurately reproduce the experimental spectra.

Furthermore, as presented in Figure S23, a few rare instances of NDoMs show extreme reshaping events in the emission spectra. Occasionally, the ZPL emission becomes very weak or even disappears, while the emission through the NIR mode is further strengthened. This indicates that there may be other microscopic mechanisms at the single-molecule level that are not captured in our model and may lead to the quasi-complete transfer of energy from the ZPL to the NIR cavity mode. Such mechanisms may include the formation of picocavities (as observed under much higher laser powers in ref 92), the possible activation of spin-forbidden transitions by magnetic modes,[104−107] or may be related to increased charge noise in the immediate vicinity of the fluorophore[108−114] due to the presence of metallic nanoparticles.

CONCLUSIONS

In summary, we experimentally studied single-molecule fluorescence reshaping due to coupling with a plasmonic nanocavity at low temperatures by investigating bare fluorophores as well as fluorophores embedded in two types of plasmonic nanocavities (NDoG and NDoM). Consistent with electromagnetic model calculations, we proposed that the pronounced emission reshaping is facilitated by a giant Purcell enhancement and associated Lamb shift, which together help emission feed into far-detuned cavity modes at NIR wavelengths (up to 850 nm). Our results may have important consequences for the design of broadband NIR single photon sources and applications in quantum communication based on single quantum emitters. For example, they suggest an alternative method for creating NIR emitters based on organic fluorophores with high quantum yield and photostability. The coupling of these emitters with plasmonic structures can lead to the development of brighter sources with tailored spectra. Importantly, whereas fluorophore line width is vastly dominated by pure dephasing under usual conditions, our analysis suggests that lifetime-limited emission could be achievable within a suitably designed nanocavity, which opens prospects for the creation of indistinguishable single photons from commercial dye molecules.[115−119]

METHODS

Sample Fabrication. Gold NDs were assembled by means of a rectangular DNA origami.[44] The DNA-origami structure was designed using CaDNAno software[120] and visualized for twist correction using CanDo.[121] It consists of a square lattice design that folds into a 2-layer sheet (2LS) of size ~60 × 50 × 5 nm^3 with one ATTO 594 or ATTO 643 fluorophore in the center. Eight handles of Poly-A15 have been extended from each side of the structure so that it could bind two 60 nm gold nanoparticles surface-functionalized with Poly-T8/18 (Biomers GmbH). The handles have been designed so that the

https://doi.org/10.1021/acsnano.4c09829
ACS Nano 2025, 19, 3172−3184

attached nanoparticles are located in the center of the structure with a single fluorophore between them (see Figure S1 for a schematic and a list of staples). For the structures assembling a single nanoparticle, a DNA-origami structure containing handles only on one side (corresponding to the fluorophore side) was assembled.

DNA-origami folding was carried out by mixing the M13mp18 scaffold (20 nM) with unmodified (200 nM) and modified (handles and fluorophore, 2000 nM) staples in a 1× TAE buffer containing 12 mM $MgCl_2$. Unmodified staples were purchased from Integrated DNA Technologies IDT, modified ones from Biomers GmbH. The use of scaffold-to-staple ratios of 1:10 and 1:100 guarantees complete integration of the staples in the structure, especially in the case of the handle strands and fluorophore. For folding, the solution was first heated up to 75 °C and then ramped down to 25 °C at the rate of 1 °C every 20 min. The folded DNA-origami structures were purified from excess staple strands by gel electrophoresis using a 1% agarose gel (LE Agarose, Biozym Scientific GmbH) in a 1× TAE buffer with 12 mM $MgCl_2$ for 2.5 h at 70 V. The appropriate band containing the targeted 2LS origami was cut out and squeezed using coverslips wrapped in parafilm. The concentration was determined via UV−vis absorption spectroscopy (Nanodrop).

For binding to DNA origami, gold nanoparticles were functionalized with a mix of Poly-T8 and Poly-T18 DNA strands (Biomers GmbH) complementary to Poly-A15 on the surface of DNA origami. First, 125 μL of thiolated DNA (100 μL of Poly-T8 and 25 μL of Poly-T18) was activated with 50 μM TCEP for 1 h in order to break disulfide bonds between SH-DNA strands. Then, activated DNA strands were mixed with 312.5 μL of 0.1% SDS solution of 60 nm gold nanoparticles of OD 20, adjusted to 1 mM NaCl, and frozen overnight.[122] Afterward, DNA-functionalized nanoparticles were purified from an excess of DNA strands using gel electrophoresis (1% agarose gel, 2 h, 100 V). This step also ensures the removal of any self-aggregated dimer formed during NP functionalization. The concentration of gold nanoparticles was determined via UV−vis absorption spectroscopy (Nanodrop). The purified 2LS origami was mixed with the purified gold nanoparticles using an excess of five gold nanoparticles per binding site and adding NaCl to a final concentration of 600 mM. After overnight incubation at room temperature, the excess of gold nanoparticles was removed by gel electrophoresis (running for 4.5 h), and the band containing correctly formed dimers (or the monomer band for the single nanoparticle structures) was extracted as described before.

The fabricated structures are then incubated for 30 min for electrostatic immobilization on a dielectric (commercially available glass slides) or gold substrate, rinsed two times with water, and flushed with nitrogen before measuring. Ultra-flat gold films are prepared using the template-stripping method as in ref 123 to ensure reproducible nanogaps.

Cryogenic Fluorescence Spectroscopy. Single-particle optical microscopy is performed on a home-built confocal microscope setup. The sample itself is housed within a closed-cycle optical cryostat (AttoCube AttoDry 800) and mounted on a three-axis nanopositioner (AttoCube ANP series) for precisely locating single nanoparticles for measurement. The sample temperature within the cryostat can be precisely controlled between 4 and 300 K using a combination of closed-cycle Helium pumping and resistive heating. A high-NA objective (AttoCube LT-APO 100× 0.82 NA) inside the cryostat is used to tightly focus light from a tunable continuous-wave optical parameter oscillator (Hübner C-Wave OPO) onto the sample. Light reflected from the focal spot is recollimated through the same objective. After blocking the laser line, the remnant signal of interest is focused into a spectrometer (Andor Kymera 193i) with a CCD camera (Andor iDus).

Measuring organic fluorophores requires us to tune the laser wavelength to the absorption maximum of the fluorophore and operate at safe excitation power levels. All spectra shown in our report are measured with the excitation wavelength at 590 nm for ATTO 590 and 633 nm for ATTO 643, with an excitation power of 10 μW. Single emitters are located by scanning the sample stage while acquiring the signal. When a single emitter is located, time series of spectra are acquired at the rate of 1 Hz. The length of the time series is made long enough to capture a bleaching step as well as a subsequent background signal from the same spot. Subtracting the average background allows us to extract the spectra emanating from the fluorophore in the focal spot. Only spectra from the time series showing a single bleaching step have been included in this study.

Room-Temperature Dark-Field Scattering. Dark-field spectroscopy is performed by weakly focusing (Olympus Plan N 4× 0.1NA) a white light source on the sample at a high angle (81°) to the normal. The scattered light is then collected through a high-NA objective (Olympus MPLFLN 100× 0.9NA) perpendicular to the sample plane. We used a pulsed supercontinuum white light source (NKT Photonics SuperK Compact) after scrambling its spatial coherence through a spinning diffuser to avoid strong fringes in the scattering spectra. A small percentage of the scattered light is sent to a camera to image the sample, while the remainder is sent to a spectrograph (Andor Kymera 193i) with a CCD (Andor iDus) to measure the scattering spectra.

Simulations. All simulations carried out in this work are implemented in the radio frequency (RF) module of COMSOL Multiphysics,[66] which uses the finite element method (FEM) to solve Maxwell's equations in the frequency domain. To mimic the experimental configurations, the simulations in the main text consider two gold spherical nanoparticles (modeled using the permittivity of Au from Johnson and Christy[124]) of 60 nm diameter, separated by a small gap of 4 nm. This dimer is deposited on top of a semi-infinite glass of refractive index 1.5 (NDoG configuration) or a 1.0 nm-thick dielectric layer (refractive index 1) placed over a gold substrate (NDoM configuration). To represent the DNA-origami structure containing the fluorophore, a cylinder of diameter 40 nm and refractive index 2.15[125] is placed between the two spherical nanoparticles. A detailed sketch and other configurations are presented in the Supporting Information.

The dark-field scattering of the NDoG and NDoM structures is calculated in COMSOL by configuring a background electric field corresponding to a linearly polarized plane wave (*s*- and *p*-polarizations) at an oblique incidence angle of 81° from the surface normal. No fluorophore is considered in these simulations of the scattering. To replicate the experimental collection of light through a high-NA objective, the scattered light is computed by integrating the Poynting vector over a surface area corresponding to a solid angle equivalent to an NA of 0.9. The total (Γ_{cav}) and radiative (Γ_{rad}) decay rates, as well as the Lamb shift, are computed using as a source an electric point-dipole placed in the ND gap. In the simulations of the main text, the dipole is positioned on and oriented parallel to the ND's long axis and placed 1 nm away from one of the surfaces of one nanoparticle. Γ_{cav} and the Lamb shift are calculated from the self-interaction Green's function, which gives the electric field (component aligned with the electric dipole) induced by the dipole at the same position of the dipole. Γ_{rad} is calculated as the integral of the Poynting vector evaluated in a closed spherical surface surrounding the system at a distance of 1.6 μm. Γ_{cav} and Γ_{rad} are then normalized to the same quantities obtained with the dipole immersed in an infinite space made of DNA (refractive index 2.15). The full simulation environment for all calculations consisted of a sphere with a radius of 2000 nm surrounded by a 400 nm-thick perfectly matched layer. Tetrahedral elements were used to mesh all domains, with the maximum mesh element size kept below $\lambda/10$, where λ is the wavelength of the excitation. For elements corresponding to the dimers and the DNA cylinder, a finer mesh size was used. Additionally, the dipole source was surrounded by a sphere with the same refractive index of DNA and a diameter equal to the gap size (4 nm) to ensure a sufficiently fine grid in the proximity of the dipole source. The mesh of the sphere surrounding the dipole source was smaller than 1.2 nm. Mesh sizes in the entire set of calculations were systematically verified to ensure that convergence was achieved.

https://doi.org/10.1021/acsnano.4c09829
ACS Nano 2025, 19, 3172−3184

ASSOCIATED CONTENT

Data Availability Statement

Data Availability statement: data and codes supporting this publication are available on the Zenodo repository 10.5281/zenodo.14524514.

Supporting Information

The Supporting Information is available free of charge at https://pubs.acs.org/doi/10.1021/acsnano.4c09829.

Further simulation results and experimental data supporting our conclusions (PDF)

AUTHOR INFORMATION

Corresponding Authors

Ruben Esteban − *Centro de Física de Materiales CFM-MPC, 20018 Donostia-San Sebastián, Spain; Donostia International Physics Center (DIPC), 20018 Donostia-San Sebastián, Spain;* orcid.org/0000-0002-9175-2878; Email: ruben.esteban@ehu.eus

Guillermo P. Acuna − *Department of Physics, University of Fribourg, 1700 Fribourg, Switzerland;* orcid.org/0000-0001-8066-2677; Email: guillermo.acuna@unifr.ch

Christophe Galland − *Institute of Physics, Ecole Polytechnique Fédérale de Lausanne (EPFL), 1015 Lausanne, Switzerland; Center of Quantum Science and Engineering, Swiss Federal Institute of Technology Lausanne (EPFL), 1015 Lausanne, Switzerland;* orcid.org/0000-0001-5627-0796; Email: chris.galland@epfl.ch

Authors

Sachin Verlekar − *Institute of Physics, Ecole Polytechnique Fédérale de Lausanne (EPFL), 1015 Lausanne, Switzerland*

Maria Sanz-Paz − *Department of Physics, University of Fribourg, 1700 Fribourg, Switzerland*

Mario Zapata-Herrera − *Centro de Física de Materiales CFM-MPC, 20018 Donostia-San Sebastián, Spain; Donostia International Physics Center (DIPC), 20018 Donostia-San Sebastián, Spain*

Mauricio Pilo-Pais − *Department of Physics, University of Fribourg, 1700 Fribourg, Switzerland;* orcid.org/0000-0001-9803-7132

Karol Kołątaj − *Department of Physics, University of Fribourg, 1700 Fribourg, Switzerland;* orcid.org/0000-0001-9167-0672

Javier Aizpurua − *Donostia International Physics Center (DIPC), 20018 Donostia-San Sebastián, Spain; Ikerbasque, Basque Foundation for Science, 48013 Bilbao, Spain; Dept. of Electricity and Electronics, University of the Basque Country (UPV/EHU), 48940 Leioa, Spain;* orcid.org/0000-0002-1444-7589

Complete contact information is available at: https://pubs.acs.org/10.1021/acsnano.4c09829

Author Contributions

○S.V., M.S.-P., and M.Z.-H. contributed equally.

Notes

The authors declare no competing financial interest.

ACKNOWLEDGMENTS

This work received funding from the European Union's Horizon 2020 research and innovation program under Grant Agreement No. 820196 (ERC CoG QTONE). C.G. also acknowledges the support from the Swiss National Science Foundation (project numbers 170684 and 198898). M.Z.-H., R.E., and J.A. acknowledge funding from grant PID2022-139579NB-I00 funded by MICIU/AEI/10.13039/501100011033 and by "ERDF/EU A way of making Europe" from grant no. IT 1526-22 from the Basque Government for consolidated groups of the Basque University, as well as by the European Union (NextGenerationEU) through the Complementary Plans (Grant No. PRTR-C17.I1) promoted by the Ministry of Science and Innovation within the Recovery, Transformation, and Resilience Plan of Spain, and part of the activities of the IKUR strategy of the Department of Education promoted by the Department of Education of the Basque Government. G.P.A. acknowledges support from the Swiss National Science Foundation (200021_184687) and from the National Center of Competence in Research Bio-Inspired Materials NCCR (51NF40_182881).

REFERENCES

(1) Bharadwaj, P.; Deutsch, B.; Novotny, L. Optical Antennas. *Advances in Optics and Photonics* **2009**, *1*, 438−483.

(2) Baumberg, J. J.; Aizpurua, J.; Mikkelsen, M. H.; Smith, D. R. Extreme nanophotonics from ultrathin metallic gaps. *Nat. Mater.* **2019**, *18*, 668−678.

(3) Prodan, E.; Radloff, C.; Halas, N. J.; Nordlander, P. A Hybridization Model for the Plasmon Response of Complex Nanostructures. *Science* **2003**, *302*, 419−422.

(4) Kinkhabwala, A.; et al. Large single-molecule fluorescence enhancements produced by a bowtie nanoantenna. *Nat. Photonics* **2009**, *3*, 654−657.

(5) Chikkaraddy, R.; et al. Single-molecule strong coupling at room temperature in plasmonic nanocavities. *Nature* **2016**, *535*, 127−130.

(6) Puchkova, A.; et al. DNA Origami Nanoantennas with over 5000-fold Fluorescence Enhancement and Single-Molecule Detection at 25 μM. *Nano Lett.* **2015**, *15*, 8354−8359.

(7) Punj, D.; et al. A plasmonic 'antenna-in-box' platform for enhanced single-molecule analysis at micromolar concentrations. *Nat. Nanotechnol.* **2013**, *8*, 512−516.

(8) Russell, K. J.; Liu, T.-L.; Cui, S.; Hu, E. L. Large spontaneous emission enhancement in plasmonic nanocavities. *Nat. Photonics* **2012**, *6*, 459−462.

(9) Akselrod, G. M.; et al. Probing the mechanisms of large Purcell enhancement in plasmonic nanoantennas. *Nat. Photonics* **2014**, *8*, 835−840.

(10) Luo, Y.; et al. Purcell-enhanced quantum yield from carbon nanotube excitons coupled to plasmonic nanocavities. *Nat. Commun.* **2017**, *8*, 1413.

(11) Hoang, T. B.; Akselrod, G. M.; Mikkelsen, M. H. Ultrafast Room-Temperature Single Photon Emission from Quantum Dots Coupled to Plasmonic Nanocavities. *Nano Lett.* **2016**, *16*, 270−275.

(12) Hoang, T. B.; et al. Ultrafast spontaneous emission source using plasmonic nanoantennas. *Nat. Commun.* **2015**, *6*, 7788.

(13) Flauraud, V.; et al. In-Plane Plasmonic Antenna Arrays with Surface Nanogaps for Giant Fluorescence Enhancement. *Nano Lett.* **2017**, *17*, 1703−1710.

(14) Marquier, F.; Sauvan, C.; Greffet, J.-J. Revisiting quantum optics with surface plasmons and plasmonic resonators. *ACS photonics* **2017**, *4*, 2091−2101.

(15) Le Ru, E. C.; et al. Mechanisms of Spectral Profile Modification in Surface-Enhanced Fluorescence. *J. Phys. Chem. C* **2007**, *111*, 16076−16079.

(16) Bakker, R. M.; et al. Enhanced localized fluorescence in plasmonic nanoantennae. *Appl. Phys. Lett.* **2008**, *92*, No. 043101.

(17) Tanaka, K.; Plum, E.; Ou, J. Y.; Uchino, T.; Zheludev, N. I. Multifold Enhancement of Quantum Dot Luminescence in Plasmonic Metamaterials. *Phys. Rev. Lett.* **2010**, *105*, No. 227403.

(18) Saemisch, L.; Liebel, M.; van Hulst, N. F. Control of Vibronic Transition Rates by Resonant Single-Molecule-Nanoantenna Coupling. *Nano Lett.* **2020**, *20*, 4537−4542.
(19) Paulo, P. M. R.; et al. Enhanced Fluorescence of a Dye on DNA-Assembled Gold nanodimers Discriminated by Lifetime Correlation Spectroscopy. *J. Phys. Chem. C* **2018**, *122*, 10971−10980.
(20) Lee, S. A.; Biteen, J. S. Spectral Reshaping of Single Dye Molecules Coupled to Single Plasmonic Nanoparticles. *J. Phys. Chem. Lett.* **2019**, *10*, 5764−5769.
(21) Wen, T.; et al. Transient Spectral Fluctuations of Single Molecules Revealed using an Optical Antenna. *J. Phys. Chem. C* **2020**, *124*, 18219−18225.
(22) Rashed, A. R.; Habib, M.; Das, N.; Ozbay, E.; Caglayan, H. Plasmon-modulated photoluminescence enhancement in hybrid plasmonic nano-antennas. *New J. Phys.* **2020**, *22*, No. 093033.
(23) Lu, X.; Punj, D.; Orrit, M. Two-Photon-Excited Single-Molecule Fluorescence Enhanced by Gold Nanorod Dimers. *Nano Lett.* **2022**, *22*, 4215−4222.
(24) Ringler, M.; et al. Shaping Emission Spectra of Fluorescent Molecules with Single Plasmonic Nanoresonators. *Phys. Rev. Lett.* **2008**, *100*, No. 203002.
(25) Ming, T.; et al. Strong Polarization Dependence of Plasmon-Enhanced Fluorescence on Single Gold Nanorods. *Nano Lett.* **2009**, *9*, 3896−3903.
(26) Zhao, L.; Ming, T.; Chen, H.; Liang, Y.; Wang, J. Plasmon-induced modulation of the emission spectra of the fluorescent molecules near gold nanorods. *Nanoscale* **2011**, *3*, 3849−3859.
(27) Li, Z.-Q.; et al. Shaping the fluorescence emission by cavity plasmons in dielectric-metal core-shell resonators. *Appl. Phys. Lett.* **2015**, *107*, 251105.
(28) Sanz-Paz, M.; et al. DNA Origami Assembled Nanoantennas for Manipulating Single-Molecule Spectral Emission. *Nano Lett.* **2023**, *23*, 6202−6208.
(29) Rothemund, P. W. K. Folding DNA to create nanoscale shapes and patterns. *Nature* **2006**, *440*, 297−302.
(30) Liu, Y.; et al. Modular Reconfigurable DNA Origami: From Two-Dimensional to Three-Dimensional Structures. *Angew. Chem., Int. Ed.* **2020**, *59*, 23277−23282.
(31) Dey, S.; et al. DNA origami. *Nat. Rev. Methods Primers* **2021**, *1*, 1−24.
(32) Kuzyk, A.; Jungmann, R.; Acuna, G. P.; Liu, N. DNA Origami Route for Nanophotonics. *ACS Photonics* **2018**, *5*, 1151−1163.
(33) Yeşilyurt, A. T. M.; Huang, J.-S. Emission Manipulation by DNA Origami-Assisted Plasmonic Nanoantennas. *Adv. Opt. Mater.* **2021**, *9*, No. 2100848.
(34) Adamczyk, A. K.; et al. DNA Self-Assembly of Single Molecules with Deterministic Position and Orientation. *ACS Nano* **2022**, *16*, 16924−16931.
(35) Cervantes-Salguero, K.; et al. Strategies for Controlling the Spatial Orientation of Single Molecules Tethered on DNA Origami Templates Physisorbed on Glass Substrates: Intercalation and Stretching. *International Journal of Molecular Sciences* **2022**, *23*, 7690.
(36) Acuna, G. P.; et al. Distance Dependence of Single-Fluorophore Quenching by Gold Nanoparticles Studied on DNA Origami. *ACS Nano* **2012**, *6*, 3189−3195.
(37) Trofymchuk, K.; et al. Gold Nanorod DNA Origami Antennas for 3 Orders of Magnitude Fluorescence Enhancement in NIR. *ACS Nano* **2023**, *17*, 1327−1334.
(38) Holzmeister, P.; et al. Quantum yield and excitation rate of single molecules close to metallic nanostructures. *Nat. Commun.* **2014**, *5*, 5356.
(39) Zhang, T.; Gao, N.; Li, S.; Lang, M. J.; Xu, Q.-H. Single-Particle Spectroscopic Study on Fluorescence Enhancement by Plasmon Coupled Gold Nanorod Dimers Assembled on DNA Origami. *J. Phys. Chem. Lett.* **2015**, *6*, 2043−2049.
(40) Kaminska, I.; Bohlen, J.; Mackowski, S.; Tinnefeld, P.; Acuna, G. P. Strong Plasmonic Enhancement of a Single Peridinin−Chlorophyll a−Protein Complex on DNA Origami-Based Optical Antennas. *ACS Nano* **2018**, *12*, 1650−1655.
(41) Heck, C.; et al. Gold Nanolenses Self-Assembled by DNA Origami. *ACS Photonics* **2017**, *4*, 1123−1130.
(42) Dutta, A.; et al. Molecular states and spin crossover of hemin studied by DNA origami enabled single-molecule surface-enhanced Raman scattering. *Nanoscale* **2022**, *14*, 16467−16478.
(43) Simoncelli, S.; et al. Quantitative Single-Molecule Surface-Enhanced Raman Scattering by Optothermal Tuning of DNA Origami-Assembled Plasmonic Nanoantennas. *ACS Nano* **2016**, *10*, 9809−9815.
(44) Hübner, K.; et al. Directing Single-Molecule Emission with DNA Origami-Assembled Optical Antennas. *Nano Lett.* **2019**, *19*, 6629−6634.
(45) Zhu, F.; et al. DNA-Templated Ultracompact Optical Antennas for Unidirectional Single-Molecule Emission. *Nano Lett.* **2022**, *22*, 6402−6408.
(46) Yeşilyurt, A. T. M.; et al. Unidirectional Meta-Emitters Based on the Kerker Condition Assembled by DNA Origami. *ACS Nano* **2023**, *17*, 19189−19196.
(47) Hedley, G. J.; et al. Picosecond time-resolved photon antibunching measures nanoscale exciton motion and the true number of chromophores. *Nat. Commun.* **2021**, *12*, 1327.
(48) Ojambati, O. S.; et al. Quantum electrodynamics at room temperature coupling a single vibrating molecule with a plasmonic nanocavity. *Nat. Commun.* **2019**, *10*, 1049.
(49) Heintz, J.; Markešević, N.; Gayet, E. Y.; Bonod, N.; Bidault, S. Few-Molecule Strong Coupling with Dimers of Plasmonic Nanoparticles Assembled on DNA. *ACS Nano* **2021**, *15*, 14732−14743.
(50) Raab, M.; Vietz, C.; Stefani, F. D.; Acuna, G. P.; Tinnefeld, P. Shifting molecular localization by plasmonic coupling in a single-molecule mirage. *Nat. Commun.* **2017**, *8*, 13966.
(51) Bézard, M.; et al. Giant Quantum Electrodynamic Effects on Single SiV Color Centers in Nanosized Diamonds. *ACS Nano* **2024**, *18*, 6406−6412.
(52) Rosławska, A.; et al. Mapping Lamb, Stark, and Purcell Effects at a Chromophore-Picocavity Junction with Hyper-Resolved Fluorescence Microscopy. *Physical Review X* **2022**, *12*, No. 011012.
(53) Zhang, Y.; et al. Sub-nanometre control of the coherent interaction between a single molecule and a plasmonic nanocavity. *Nat. Commun.* **2017**, *8*, 15225.
(54) Duan, H.; Fernández-Domínguez, A. I.; Bosman, M.; Maier, S. A.; Yang, J. K. W. Nanoplasmonics: Classical down to the Nanometer Scale. *Nano Lett.* **2012**, *12*, 1683−1689.
(55) Kadkhodazadeh, S.; Wagner, J. B.; Kneipp, H.; Kneipp, K. Coexistence of classical and quantum plasmonics in large plasmonic structures with subnanometer gaps. *Appl. Phys. Lett.* **2013**, *103*, No. 083103.
(56) Cha, H.; Yoon, J. H.; Yoon, S. Probing Quantum Plasmon Coupling Using Gold Nanoparticle Dimers with Tunable Interparticle Distances Down to the Subnanometer Range. *ACS Nano* **2014**, *8*, 8554−8563.
(57) Pini, V.; et al. Spatially multiplexed dark-field micro-spectrophotometry for nanoplasmonics. *Sci. Rep.* **2016**, *6*, 22836.
(58) Dickreuter, S.; Kern, D. P.; Fleischer, M. Single particle dark-field spectroscopy of spherical dimers with down to sub-10 nm gaps fabricated by the annealing of nano-pillars. *Nanophotonics* **2018**, *7*, 1317−1324.
(59) Song, J.-H.; et al. Nanoelectromechanical modulation of a strongly-coupled plasmonic dimer. *Nat. Commun.* **2021**, *12*, 48.
(60) Huang, Y.; et al. Hybridized plasmon modes and near-field enhancement of metallic nanoparticle-dimer on a mirror. *Sci. Rep.* **2016**, *6*, 30011.
(61) Chen, S.; et al. How To Light Special Hot Spots in Multiparticle−Film Configurations. *ACS Nano* **2016**, *10*, 581−587.
(62) Li, G.-C.; Zhang, Y.-L.; Yuan Lei, D. Hybrid plasmonic gap modes in metal film-coupled dimers and their physical origins revealed by polarization resolved dark field spectroscopy. *Nanoscale* **2016**, *8*, 7119−7126.
(63) Yoon, J. H.; Selbach, F.; Langolf, L.; Schlücker, S. Ideal Dimers of Gold Nanospheres for Precision Plasmonics: Synthesis and

https://doi.org/10.1021/acsnano.4c09829
ACS Nano 2025, 19, 3172−3184

Characterization at the Single-Particle Level for Identification of Higher Order Modes. *Small* **2018**, *14*, No. 1702754.
(64) Meng, Y.; et al. Plasmon-Induced Optical Magnetism in an Ultrathin Metal Nanosphere-Based Dimer-on-Film Nanocavity. *Laser Photonics Rev.* **2020**, *14*, No. 2000068.
(65) Li, G.-C.; Zhang, Y.-L.; Jiang, J.; Luo, Y.; Lei, D. Y. Metal-Substrate-Mediated Plasmon Hybridization in a Nanoparticle Dimer for Photoluminescence Line-Width Shrinking and Intensity Enhancement. *ACS Nano* **2017**, *11*, 3067−3080.
(66) COMSOL AB. *COMSOL Multiphysics® v5.6*; COMSOL: Stockholm, Sweden, 2020.
(67) Reitz, M.; et al. Molecule-photon interactions in phononic environments. *Physical Review Research* **2020**, *2*, No. 033270.
(68) Ooi, C. H. R.; Chia, K. J. C. Unified master equation for molecules in phonon and radiation baths. *Sci. Rep.* **2022**, *12*, 20015.
(69) Zhao, D.; et al. Impact of Vibrational Modes in the Plasmonic Purcell Effect of Organic Molecules. *ACS Photonics* **2020**, *7*, 3369−3375.
(70) Jamshidi, Z.; Kargar, K.; Mendive-Tapia, D.; Vendrell, O. Coupling Molecular Systems with Plasmonic Nanocavities: A Quantum Dynamics Approach. *J. Phys. Chem. Lett.* **2023**, *14*, 11367−11375.
(71) Gurlek, B.; Sandoghdar, V.; Martín-Cano, D. Manipulation of Quenching in Nanoantenna−Emitter Systems Enabled by External Detuned Cavities: A Path to Enhance Strong-Coupling. *ACS Photonics* **2018**, *5*, 456−461.
(72) Wang, D.; et al. Turning a molecule into a coherent two-level quantum system. *Nat. Phys.* **2019**, *15*, 483−489.
(73) Pscherer, A.; et al. Single-Molecule Vacuum Rabi Splitting: Four-Wave Mixing and Optical Switching at the Single-Photon Level. *Phys. Rev. Lett.* **2021**, *127*, No. 133603.
(74) Zhu, W.; et al. Quantum mechanical effects in plasmonic structures with subnanometre gaps. *Nat. Commun.* **2016**, *7*, 11495.
(75) Galland, C.; Högele, A.; Türeci, H. E.; Imamoğlu, A. Non-Markovian Decoherence of Localized Nanotube Excitons by Acoustic Phonons. *Phys. Rev. Lett.* **2008**, *101*, No. 067402.
(76) Pellegrotti, J. V.; et al. Controlled Reduction of Photobleaching in DNA Origami−Gold Nanoparticle Hybrids. *Nano Lett.* **2014**, *14*, 2831−2836.
(77) Kaminska, I.; et al. Strong plasmonic enhancement of single molecule photostability in silver dimer optical antennas. *Nanophotonics* **2018**, *7*, 643−649.
(78) Ates, S.; et al. Non-resonant dot−cavity coupling and its potential for resonant single-quantum-dot spectroscopy. *Nat. Photonics* **2009**, *3*, 724−728.
(79) Suffczyński, J.; et al. Origin of the optical emission within the cavity mode of coupled quantum dot-cavity systems. *Physical review letters* **2009**, *103*, No. 027401.
(80) Hohenester, U. Cavity quantum electrodynamics with semiconductor quantum dots: Role of phonon-assisted cavity feeding. *Phys. Rev. B* **2010**, *81*, No. 155303.
(81) Hughes, S.; et al. Influence of electron-acoustic phonon scattering on off-resonant cavity feeding within a strongly coupled quantum-dot cavity system. *Phys. Rev. B* **2011**, *83*, No. 165313.
(82) Lodahl, P.; Mahmoodian, S.; Stobbe, S. Interfacing single photons and single quantum dots with photonic nanostructures. *Rev. Mod. Phys.* **2015**, *87*, 347−400.
(83) Grabenhorst, L.; Trofymchuk, K.; Steiner, F.; Glembockyte, V.; Tinnefeld, P. Fluorophore photostability and saturation in the hotspot of DNA origami nanoantennas. *Methods and Applications in Fluorescence* **2020**, *8*, No. 024003.
(84) Ito, Y.; Matsuda, K.; Kanemitsu, Y. Mechanism of photoluminescence enhancement in single semiconductor nanocrystals on metal surfaces. *Phys. Rev. B* **2007**, *75*, No. 033309.
(85) Yuan, C. T.; Yu, P.; Tang, J. Blinking suppression of colloidal CdSe/ZnS quantum dots by coupling to silver nanoprisms. *Appl. Phys. Lett.* **2009**, *94*, 243108.
(86) Wu, X.-W.; et al. Anti-bunching and luminescence blinking suppression from plasmon-interacted single CdSe/ZnS quantum dot. *Opt. Express* **2010**, *18*, 6340−6346.
(87) Wang, Z.; et al. Bright Nonblinking Photoluminescence with Blinking Lifetime from a Nanocavity-Coupled Quantum Dot. *Nano Lett.* **2024**, *24*, 1761−1768.
(88) Chen, W.; et al. Intrinsic luminescence blinking from plasmonic nanojunctions. *Nat. Commun.* **2021**, *12*, 2731.
(89) Lumdee, C.; Yun, B.; Kik, P. G. Gap-Plasmon Enhanced Gold Nanoparticle Photoluminescence. *ACS Photonics* **2014**, *1*, 1224−1230.
(90) Cai, Y.-Y.; et al. Photoluminescence of Gold Nanorods: Purcell Effect Enhanced Emission from Hot Carriers. *ACS Nano* **2018**, *12*, 976−985.
(91) Hugall, J. T.; Baumberg, J. J. Demonstrating Photoluminescence from Au is Electronic Inelastic Light Scattering of a Plasmonic Metal: The Origin of SERS Backgrounds. *Nano Lett.* **2015**, *15*, 2600−2604.
(92) Rocchetti, S.; et al. Amplified Plasmonic Forces from DNA Origami-Scaffolded Single Dyes in Nanogaps. *Nano Lett.* **2023**, *23*, 5959−5966.
(93) Yao, P.; et al. Ultrahigh Purcell factors and Lamb shifts in slow-light metamaterial waveguides. *Phys. Rev. B* **2009**, *80*, No. 195106.
(94) Hughes, S.; Yao, P. Theory of quantum light emission from a strongly-coupled single quantum dot photonic-crystal cavity system. *Opt. Express* **2009**, *17*, 3322−3330.
(95) Larkin, I. A.; Stockman, M. I.; Achermann, M.; Klimov, V. I. Dipolar emitters at nanoscale proximity of metal surfaces: Giant enhancement of relaxation in microscopic theory. *Phys. Rev. B* **2004**, *69*, No. 121403.
(96) Babaze, A.; Neuman, T.; Esteban, R.; Aizpurua, J.; Borisov, A. G. Dispersive surface-response formalism to address nonlocality in extreme plasmonic field confinement. *Nanophotonics* **2023**, *12*, 3277−3289.
(97) García de Abajo, F. J. Nonlocal Effects in the Plasmons of Strongly Interacting Nanoparticles, Dimers, and Waveguides. *J. Phys. Chem. C* **2008**, *112*, 17983−17987.
(98) Baumberg, J. J. picocavities: A Primer. *Nano Lett.* **2022**, *22*, 5859−5865.
(99) Urbieta, M.; et al. Atomic-Scale Lightning Rod Effect in Plasmonic picocavities: A Classical View to a Quantum Effect. *ACS Nano* **2018**, *12*, 585−595.
(100) Veys, K.; Escudero, D. Anti-Kasha Fluorescence in Molecular Entities: Central Role of Electron−Vibrational Coupling. *Acc. Chem. Res.* **2022**, *55*, 2698−2707.
(101) Liebel, M.; Toninelli, C.; van Hulst, N. F. Room-temperature ultrafast nonlinear spectroscopy of a single molecule. *Nat. Photonics* **2018**, *12*, 45−49.
(102) Schedlbauer, J.; et al. Ultrafast Single-Molecule Fluorescence Measured by Femtosecond Double-Pulse Excitation Photon Anti-bunching. *Nano Lett.* **2020**, *20*, 1074−1079.
(103) Clear, C.; et al. Phonon-Induced Optical Dephasing in Single Organic Molecules. *Phys. Rev. Lett.* **2020**, *124*, No. 153602.
(104) Ojambati, O. S.; et al. Breaking the Selection Rules of Spin-Forbidden Molecular Absorption in Plasmonic Nanocavities. *ACS Photonics* **2020**, *7*, 2337−2342.
(105) Duan, S.; Rinkevicius, Z.; Tian, G.; Luo, Y. Optomagnetic Effect Induced by Magnetized Nanocavity Plasmon. *J. Am. Chem. Soc.* **2019**, *141*, 13795−13798.
(106) Rusak, E.; et al. Enhancement of and interference among higher order multipole transitions in molecules near a plasmonic nanoantenna. *Nat. Commun.* **2019**, *10*, 5775.
(107) Kern, A. M.; Martin, O. J. F. Strong enhancement of forbidden atomic transitions using plasmonic nanostructures. *Phys. Rev. A* **2012**, *85*, No. 022501.
(108) Hauck, M.; et al. Locating environmental charge impurities with confluent laser spectroscopy of multiple quantum dots. *Phys. Rev. B* **2014**, *90*, No. 235306.

https://doi.org/10.1021/acsnano.4c09829
ACS Nano 2025, 19, 3172−3184

(109) Türck, V.; et al. Effect of random field fluctuations on excitonic transitions of individual CdSe quantum dots. *Phys. Rev. B* **2000**, *61*, 9944−9947.
(110) Shkarin, A.; et al. Nanoscopic Charge Fluctuations in a Gallium Phosphide Waveguide Measured by Single Molecules. *Phys. Rev. Lett.* **2021**, *126*, No. 133602.
(111) Segura, J. M.; Zumofen, G.; Renn, A.; Hecht, B.; Wild, U. P. Tip-induced spectral dynamics of single molecules. *Chem. Phys. Lett.* **2001**, *340*, 77−82.
(112) Bauer, M.; Kador, L. Electric-field effects of two-level systems observed with single-molecule spectroscopy. *J. Chem. Phys.* **2003**, *118*, 9069−9072.
(113) Gerhardt, I.; Wrigge, G.; Sandoghdar, V. Control and imaging of single-molecule spectral dynamics using a nano-electrode. *Mol. Phys.* **2009**, *107*, 1975−1979.
(114) Houel, J.; et al. Probing Single-Charge Fluctuations at a GaAs/AlAs Interface Using Laser Spectroscopy on a Nearby InGaAs Quantum Dot. *Phys. Rev. Lett.* **2012**, *108*, No. 107401.
(115) Varoutsis, S.; et al. Restoration of photon indistinguishability in the emission of a semiconductor quantum dot. *Phys. Rev. B* **2005**, *72*, No. 041303.
(116) Gazzano, O.; et al. Bright solid-state sources of indistinguishable single photons. *Nat. Commun.* **2013**, *4*, 1425.
(117) Somaschi, N.; et al. Near-optimal single-photon sources in the solid state. *Nat. Photonics* **2016**, *10*, 340−345.
(118) Tomm, N.; et al. A bright and fast source of coherent single photons. *Nat. Nanotechnol.* **2021**, *16*, 399−403.
(119) Husel, L.; et al. Cavity-enhanced photon indistinguishability at room temperature and telecom wavelengths. *Nat. Commun.* **2024**, *15*, 3989.
(120) Douglas, S. M.; et al. Rapid prototyping of 3D DNA-origami shapes with CaDNAno. *Nucleic Acids Res.* **2009**, *37*, 5001−5006.
(121) Kim, D.-N.; Kilchherr, F.; Dietz, H.; Bathe, M. Quantitative prediction of 3D solution shape and flexibility of nucleic acid nanostructures. *Nucleic Acids Res.* **2012**, *40*, 2862−2868.
(122) Liu, B.; Liu, J. Freezing Directed Construction of Bio/Nano Interfaces: Reagentless Conjugation, Denser Spherical Nucleic Acids, and Better Nanoflares. *J. Am. Chem. Soc.* **2017**, *139*, 9471−9474.
(123) Ahmed, A.; et al. Structural Order of the Molecular Adlayer Impacts the Stability of Nanoparticle-on-Mirror Plasmonic Cavities. *ACS Photonics* **2021**, *8*, 1863−1872.
(124) Johnson, P. B.; Christy, R. W. Optical Constants of the Noble Metals. *Phys. Rev. B* **1972**, *6*, 4370−4379.
(125) Thacker, V. V.; et al. DNA origami based assembly of gold nanoparticle dimers for surface-enhanced Raman scattering. *Nat. Commun.* **2014**, *5*, 3448.

https://doi.org/10.1021/acsnano.4c09829
ACS Nano 2025, 19, 3172−3184